IN SITU SYNCHROTRON MICROTOMOGRAPHY REVEALS PLY THICKNESS AND NANOREINFORCEMENT EFFECTS ON HYBRID COMPOSITE PROGRESSIVE DAMAGE

Reed Kopp[1], Xinchen Ni[2], Carolina Furtado[3], Jeonyoon Lee[4], Estelle Kalfon-Cohen[5], Kentaro Uesugi[6], Mike Kinsella[7], Mark N. Mavrogordato[8], Ian Sinclair[9], S. Mark Spearing[10], Pedro P. Camanho[11], and Brian L. Wardle[12]

[1] Dept. of Aeronautics and Astronautics, Massachusetts Institute of Technology, Cambridge, USA, ATA Engineering, Inc. Herndon, VA, USA, Web: ata-e.com, reed.kopp@ata-e.com
[2] Dept. of Mechanical Engineering, Massachusetts Institute of Technology, Cambridge, USA
[3] DEMec, Faculdade de Engenharia da Universidade do Porto, Porto, Portugal;
Instituto de Ciência e Inovação em Engenharia Mecânica e Engenharia Industrial, Porto, Portugal
[4] Dept. of Aeronautics and Astronautics, Massachusetts Institute of Technology, Cambridge, USA
[5] Dept. of Aeronautics and Astronautics, Massachusetts Institute of Technology, Cambridge, USA
[6] Japan Synchrotron Radiation Research Institute/SPring-8, Hyogo, Japan
[7] Teijin Carbon America, Inc., Rockwood, USA
[8] Faculty of Engineering and the Environment, University of Southampton, Southampton, UK
[9] Faculty of Engineering and the Environment, University of Southampton, Southampton, UK
[10] Faculty of Engineering and the Environment, University of Southampton, Southampton, UK
[11] DEMec, Faculdade de Engenharia da Universidade do Porto, Porto, Portugal;
Instituto de Ciência e Inovação em Engenharia Mecânica e Engenharia Industrial, Porto, Portugal
[12] Dept of Aeronautics and Astronautics, Massachusetts Institute of Technology, Cambridge, USA, Dept. of Mechanical Engineering, Massachusetts Institute of Technology, Cambridge, USA,
Web: aeroastro.mit.edu, wardle@mit.edu

Keywords: Carbon nanotube/carbon fiber/epoxy composite, Thin-ply, 3D progressive damage

ABSTRACT

The effects on 4D progressive damage in carbon (micro) fiber reinforced plastic/polymer (CFRP) composite laminates of ply thickness, nanostitch (interlaminar nanoreinforcement technique involving high-density forests of vertically aligned carbon nanotubes, forming a hybrid composite laminate), and their coupling are studied. Particularly, the 3D strengthening and toughening mechanisms of each laminate configuration are elucidated using *in situ* synchrotron radiation computed tomography (SRCT) of cross-ply (prone to delaminations) double edge-notched tension (DENT) configurations via semi-automatic damage segmentation. For enhanced reconstruction of features in 90° laminae that are usually blurred by being oriented parallel to the X-ray beam, a wedge fixture was developed to implement a 20° loading rig cant. At beamline 47XU (BL47XU) of the Super Photon ring-8 GeV (SPring-8) facility in Japan, SRCT experiments were conducted for four different laminate configurations, including baseline and nanostitched variants coupled with thin- and thick-ply (4× thicker ply vs. thin-ply) variants. The highest ultimate tensile strength (UTS) is achieved by the hybridized nanostitched thick-ply laminate (15% increase over thick-ply baseline, >20% increase over thin-ply laminates), which exhibits an effective combination of notch-blunting intralaminar matrix damage and greatly suppressed interlaminar matrix damage (4.3× less surface area at 90% UTS). Regarding ply thickness (baseline) effects, an 8% UTS increase is exhibited in thick-ply laminates over the thin-ply, explained mechanistically by the observed characteristic progressive damage states being dominated in thick-ply laminates by notch-blunting inter- and intra-laminar matrix damage (advantageous here) and in thin-ply laminates by fiber breakage and diffuse matrix damage (disadvantageous here). A 6% UTS decrease is also found for the nanostitched vs. baseline thin-ply laminates, emphasizing the need for such mechanistic studies, as these combined nanostitch and thin-ply technologies are not beneficial in all cases. The new CFRP failure insights presented here may guide hybrid- and geometric-based mechanical enhancement methods and improve physics-based damage modeling.

1 INTRODUCTION

Laminated advanced composite materials consisting of carbon (micro) fiber reinforced plastic/polymer (CFRP) can be integrated into lighter-weight and higher-performance structures than traditional engineering materials, facilitated by the relative designability of superior CFRP mass-specific stiffness and strength properties (dominated by fibers) for specific applications (*e.g.*, aerospace vehicle primary components). Though, relatively low CFRP transverse and shear properties (dominated by the matrix) can often give rise to difficult-to-understand pre-ultimate complex failure mechanism, limiting more widespread, cost-effective adoption. Thus, several published works have reported the integration of out-of-plane fibers (*e.g.*, mm-scale Z-pins [1], micro-tufts [2], and 3D micro-weaves [3]), given the relatively high efficiency of fibrous reinforcement types, to prevent or delay ply-ply delaminations and other matrix-limited mechanical behavior. However, this through-thickness reinforcement by microscale (and larger) fibers also generally reduces in-plane properties. In response, this study employs a nanoscale approach (forming a hybrid multiscale/hierarchical composite) to reinforce inferior interlaminar regions in the out-of-plane direction using aligned carbon-nanotubes (A-CNTs), known as nanostitching, which has demonstrated various significant improvements in both in- and out-of-plane strength and toughness properties of several CFRP material systems [4–6].

As an alternative composite laminate design approach, thin-ply CFRP materials, notionally with a ply thickness less than 100 µm, in comparison to thicknesses of ~125–150 µm for standard aerospace-grade unidirectional prepreg plies, have recently demonstrated a range of strengthening and toughening improvements associated with an *'in situ'* geometric size effect that decreases the driving force for matrix cracking/fracture and consequently prevents or delays the onset and progression of both ply cracking (intralaminar matrix damage) and delamination (interlaminar matrix damage), across a range of loading conditions [7–10]. Particularly, as a result of a given ply being constrained by neighboring off-aligned plies, the in-plane shear, transverse shear, transverse compressive, and transverse tensile ultimate strengths of the embedded ply are increased relative to those of an isolated ply due to the change or delay in failure mode. However, potential disadvantages of thin-ply laminates include the presence of more ply/ply interfaces (for a given laminate thickness) and less ductile failure evolution prior to ultimate failure. For example, as reported for notched tension [11] and impact loading [10], thin-ply laminates are not beneficial for mechanical performance over conventional-thickness-ply laminates in all cases, especially those in which diffuse damage and brittle failure are disadvantageous. By addressing some of these drawbacks via the integration of nanostitch, nanostitched (hybrid) thin-ply laminates were found to exhibit a synergistic improvement in interlaminar shear strength as tested by short beam shear [12]. Yet, the detailed understanding of 3D strengthening and toughening mechanisms of ply thickness, nanostitch, and their coupling is presently inadequate, since, for example, the notched tensile testing of quasi-isotropic laminates was unable to activate interlaminar failure modes targeted by nanostitch [11].

Additionally, prior such studies have relied on traditional/standard experimental characterizations (*e.g.*, microscopy, lab-based X-ray micro-computed tomography [µCT], ultrasonic scanning) of progressive damage/failure effects caused by these technologies, further limiting mechanistic insights. As a state-of-the-art higher-fidelity experimental characterization technique that is able to capture complex progressive failure mechanisms involving multiple scales and interacting modes, *in situ* synchrotron radiation CT (SRCT) has provided new data-driven understanding of the 3D failure evolution of CFRP laminates by combining high-resolution interior imaging and mechanical loading [13,14]. SRCT enables non-destructive imaging and quantitative characterization of the laminate interior, allowing fiber/matrix constituent morphology, manufacturing defects, and damage mechanisms to be clearly observed at sub-micron voxel size and followed over time (*i.e.*, 4D assessment) as a function of applied load. Among several advantages over laboratory-based X-ray µCT for composites imaging, SRCT offers higher resolutions, higher signal-to-noise ratios, and faster scan speeds.

In this study, we characterize the fundamental effects of ply thickness (*n.b.*, an intermediate ply thicknesses was tested similarly in prior work [15]), nanostitch, and their coupling on 4D (3 spatial dimensions and 1 temporal dimension) failure mechanisms of aerospace-grade CFRP composite laminates using *in situ* SRCT in a canted loading configuration that permits clear nondestructive visualization of 4D progressive damage and constituents during mechanical loading.

2 EXPERIMENTAL METHODS

In this section, we present the experimental methods for manufacturing of nanostitched CFRP laminates, fabrication of double edge-notched tension (DENT) specimens, *ex situ* mechanical testing for load step calibration, and *in situ* SRCT coupled with mechanical loading for damage observation. These experimental methodology use here is closely associated with similar conventional CFRP DENT studies [13,14], with an exception being that our *in situ* loading fixture is canted from vertical, as presented conceptually in [16], to promote sharp reconstruction of all interior features by off-aligning them with respect to the X-ray beam orientation. More comprehensive experimental details are reported in [17].

2.1 Manufacturing of Nanostitched CFRP Laminates with Aligned Carbon Nanotube Forests

The manufacturing of nanostitched laminates adhered to the procedures for chemical vapor deposition-based growth at atmospheric pressure and A-CNT forest height characterization via microscopy (±2 μm resolution) identical to those described in [17], which were based on other previously published procedures [17,18]. The multi-walled A-CNT forests synthesized were 20 ± 5 μm tall and had a forest volume fraction of ~1%. Toho Tenax HTS40/Q-1112 (54 μm nominal cured ply thickness, 39.9% nominal resin weight content) prepreg was the thin-ply CF/epoxy material system studied here, similar to prior studies [11,12,15,17]. The same procedures from these prior studies were implemented here for both A-CNT transfer onto tacky uncured ply surfaces (wafer-to-ply transfer rate of greater than 90%) and curing via autoclave under vacuum. For each ply thickness, both baseline and nanostitch specimen types were prepared from the same laminate, noting that only two 30 mm × 40 mm regions consisted of nanostitched interfaces in each 150-mm × 150-mm laminate. Of relevance here based on the identical CFRP system and nanostitching technique used, a negligible laminate thickness increase (within standard error) linked to nanostitching was found, due to autoclave pressurization [12]. All specimens used in this study were autoclave cured in the same cure session.

2.2 Preparation of Scaled-Down DENT Specimens

In this study, a technique called ply blocking was used to vary ply thickness (established by various prior works, *e.g.*, [10,12,19]), for which adjacent thin plies with identical orientation are grouped into one blocked (effective) ply, which is justified given that ply/ply interfaces within a ply block that exist prior to curing are effectively eliminated during curing/consolidation due to fiber nesting in aligned plies. Overviewed in Table 1 are the ply-thickness configurations and associated cross-ply layup strategies that implement ply blocking of thin-ply laminae, wherein we note that 'Thin' and 'Thick' are in the scope of the current study; 'Intmed', which is most similar to a traditional aerospace-grade CFRP unidirectional prepreg ply that generally has a nominal cured ply thickness of ~130 μm, is reported in a prior similar study [15]. Thus, note that the 'Thick' effective ply thickness is similar to two repeated standard-thickness aerospace-grade plies, a layup practice that is considered permissible in industry. For hybrid laminates, each effective ply/ply interface was nanostitched. Shown in Figure 1 is a representative tomogram of each laminate configuration (classified by ply thickness and baseline vs. nanostitched/hybrid) acquired via SRCT at ~0% ultimate tensile strength (UTS), wherein nested ply blocks and negligible interlaminar thickness differences in nanostitched ply/ply interfaces are observed. As stated, Intmed was studied in prior work [15] but is included in Figure 1 for comparison.

Table 1: Ply thickness control in cross-ply laminates via a ply blocking technique, where Thin and Thick (bold text) are the subjects of the current paper. All laminates consist of 16 plies of the unidirectional thin-ply prepreg system, and repeated plies are grouped into a single effective ply.

Ply thickness configuration	Ply stacking sequence	Thin-ply count in each effective ply [#]	Nominal effective ply thickness [μm]	Thin-ply count in each laminate [#]
Thin	$[90^o/0^o]_{4S}$	**1**	**54**	**16**
Intmed	$[90^o_2/0^o_2]_{2S}$	2	108	16
Thick	$[90^o_4/0^o_4]_S$	**4**	**216**	**16**

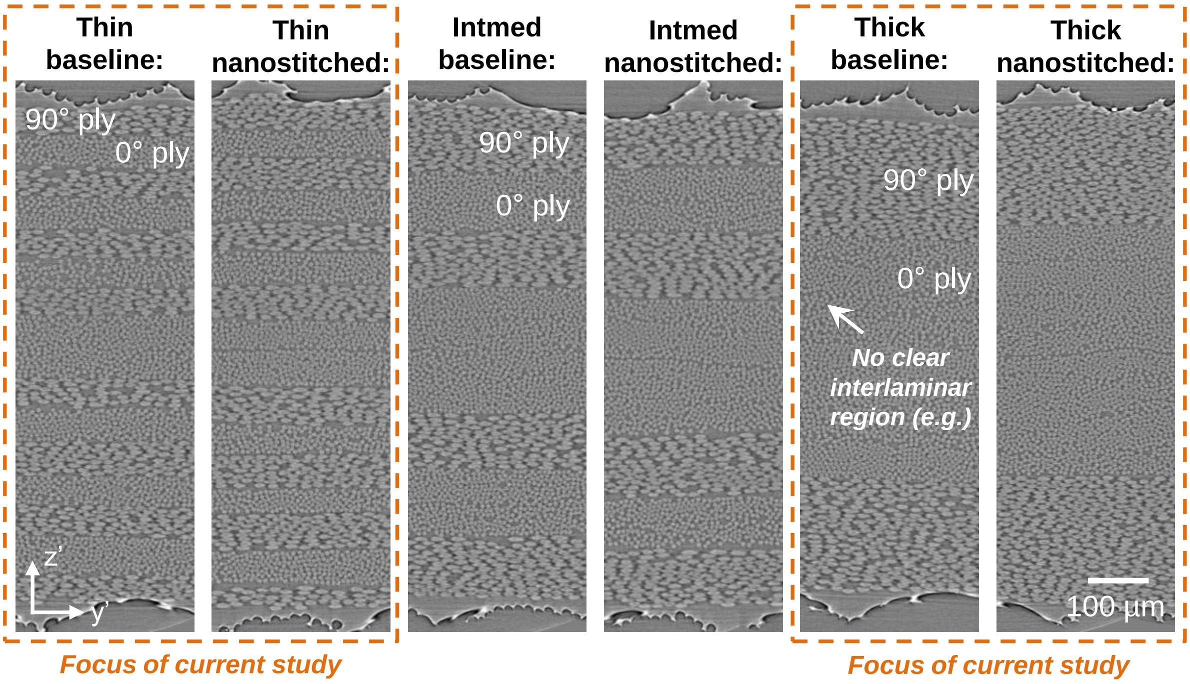

Figure 1: CFRP laminate configurations studied here based on ply thickness and nanostitching: sample SRCT tomograms of post-cure as-manufactured cross-sections of the 6 laminate configurations, where Thin and Thick are the foci of the current paper, confirming the efficacy of ply blocking to achieve effectively thicker uniform plies that lack clear interlaminar regions between repeated plies. Nanostitching (not visible via SRCT here) was integrated into each effective ply/ply interface.

DENT specimens (shown in Figure 2) were prepared with the following geometry: length of 39 mm, grip-section width of 4 mm, nominal thickness of 1 mm, and two 0.8-mm radius edge notches centered lengthwise. The coupon geometry and test setup were selected in this study due to their reliability for focusing damage to predictable, SRCT-visible regions (motivated by [13,14]). A high-precision waterjetting (Omax 2652 Jet Machining Center; 0.01-in tool offset) was used to machine the scaled-down DENT specimens, noting that Thin specimens were found to require top and bottom polymer plate reinforcements to absorb the exterior surface impingements of the water jet and thus mitigate specimen manufacturing damage. Although not required for Intmed and Thick specimens, all laminates were sandwiched by a 2-mm thick fiberglass bottom support plate and a 1-mm thick top polycarbonate plate prior to waterjet cutting for which motion was constrained to be normal to 90° ply direction. Waterjetting concluded the specimen preparation process, as no polishing was conducted, noting that the scaled-down quality refers to standard-sized notched/holed specimens typically featuring an ~3-mm radius hole.

2.3 *Ex Situ* DENT Testing for Strength Calibration

To obtain/calibrate DENT ultimate tensile strength (UTS) values for each ply thickness configuration, *ex situ* testing was conducted using the *in situ* 5-kN uniaxial loading fixture (Deben CT5000), which was not canted during *ex situ* testing for simplicity. The UTS values were calculated via Equation (1) and used for load step determination during *in situ* testing. Additional details describing the *ex situ* UTS experimental test setup and specimen geometry are shown in [17].

$$\sigma_{\mathrm{UTS}} = \frac{P_{\max}}{w_{\mathrm{DENT}} \times t_{\mathrm{DENT}}} \tag{1}$$

where $P_{\max}$, w_{DENT}, and t_{DENT} are the maximum applied tensile load observed during testing, the width, and the thickness of the 0.8-mm radius DENT specimen used in this study, respectively. In this study, w_{DENT} refers to the minimum notch section (ligament) width measured for each specimen, and UTS (used interchangeably with σ_{DENT}) refers to Equation (1).

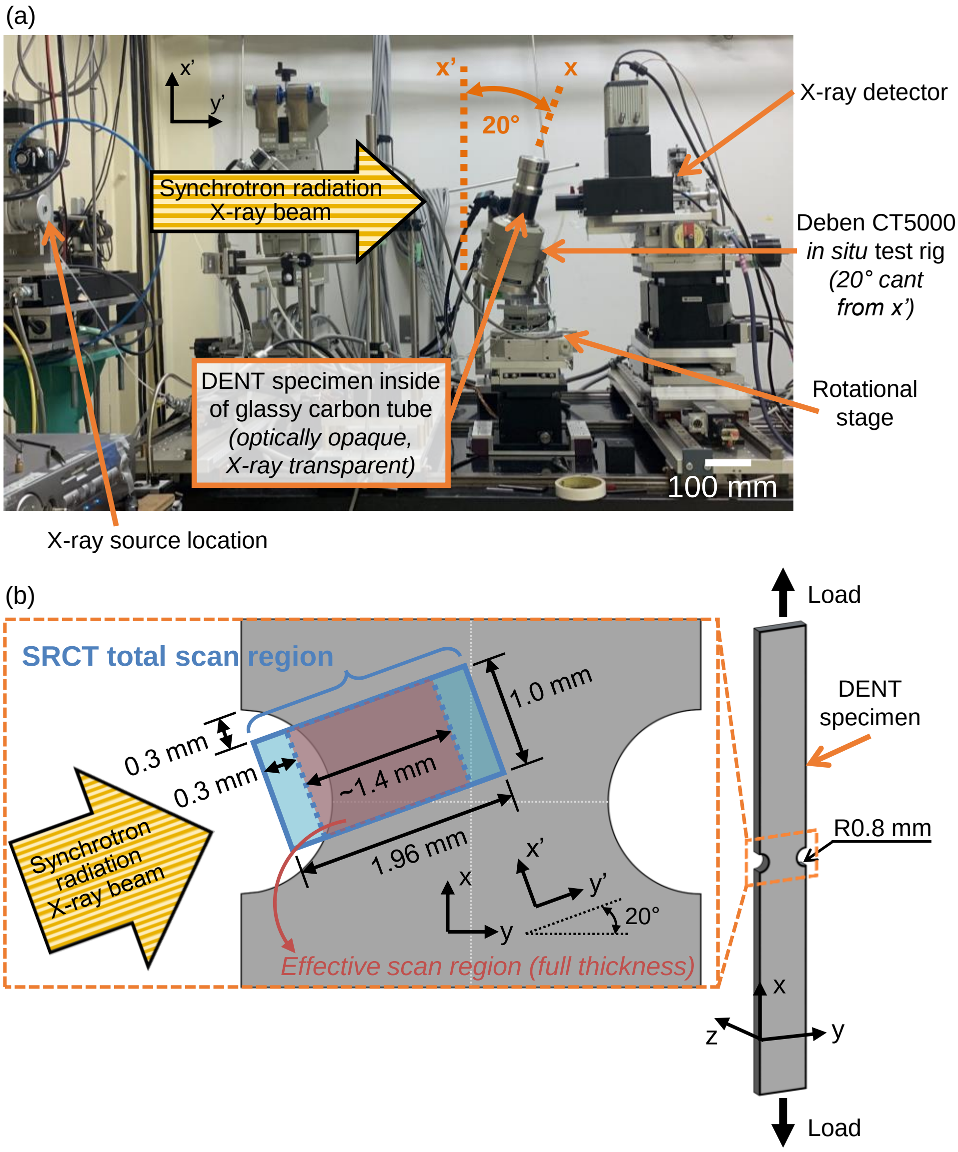

Figure 2: *In situ* DENT test setup for SRCT at the Super Photon ring-8 GeV (SPring-8) beamline 47XU (BL47XU): (a) test setup details from a side view showing the entire source-specimen-detector configuration. (b) Zoomed-in illustration of the SRCT scan region (total field-of-view [FoV], shown in blue) location, which captures concentrated damage, relative to a single 20°-canted DENT specimen notch (thin white lines delineate specimen quadrants). Note that the total FoV is comprised of four standard FoV (cylindrical) scans that were precisely positioned for subsequent reconstructed scan co-registration (manual overlap techniques employed here). A custom wedge base plate was developed to cant the loading rig by 20° from vertical, which enhanced the imaging of typically X-ray-beam-aligned internal features. No effect on the loading operation was observed due to the test fixture canting.

2.4 *In Situ* Canted DENT Testing using SRCT

In situ uniaxial DENT testing was conducted employing BL47XU at SPring-8, Japan in displacement control (0.3 mm/minute, 2 Hz sample rate) at load steps (common to all specimen types) of ~0% (unloaded), 70%, 80%, and 90% of the DENT UTS (baseline UTS for a given ply thickness configuration is herein denoted as UTS in the context of load steps and refers to the calibrated mean baseline *ex situ* UTS [be-UTS]). SRCT scans captured one of the two notched regions in each specimen. Shown in Figure 2 are the 20°-canted *in situ* UTS test setup and DENT specimen geometry. The original canting concept is attributed to our collaborators at the University of Southampton, UK [16]. For this study, a custom wedge plate was prepared to off-align the loading rig by a constant 20° cant angle measured from vertical, to facilitate sharp imaging of internal specimen features typically aligned with the X-ray beam plane. Each load step endured an average of ~30 minutes, consisting of time for load application, stress relaxation (typically less than 10 MPa) at fixed displacement to reduce blurring, and scan center positioning and acquisition for four overlapping standard-sized FoVs (each 2,048 pixels × 2,048 pixels × 2,048 pixels). The displacement remained fixed after the target load step achievement and until all scans were finished at each load step; this process was then repeated for all load steps. The four scan positions were distributed only along the specimen width and overlapped such that both full specimen thickness and maximum widthwise FoV were captured (constrained by the beam cross-section available at BL47XU). After the last load step, the specimens were loaded to ultimate failure, resulting in the *in situ* DENT UTS. In summary, the SRCT scan acquisitions and reconstructions were performed using the following details: 23 keV X-ray energy, 70 ms exposure, 1800 radiographic projections (180° angular range), 0.49 µm isotropic voxel size, 68 mm propagation distance (edge-enhancing phase contrast), and 1.96 mm × 1.0 mm × 1.0 mm total FoV. Further details are provided in [17].

Following X-ray radiograph acquisition, BL47XU standard codes were implemented that incorporate the single scan reconstruction and normalization code directory by Kentaro Uesugi (SPring-8/JASRI) [20]. Following scan normalization, conversion to 8-bit gray value images, and cropping to remove exterior regions using Fiji ImageJ, manual scan co-registration (without interpolation) was done using Avizo 2019.2 commercial software to produce one stitched FoV for each load step.

Lastly, SRCT scan segmentation of intralaminar and interlaminar matrix damage was performed by a trained human using Avizo 2020.2 commercial software, adhering to the semi-automatic technique based on seeded region growing described in [11,17], using a grayscale threshold range of [0, 30] generally and [0, 60] in matrix damage regions with low phase contrast (*e.g.*, cracks with large opening displacements) to enhance accuracy in capturing interior fracture surfaces. The relatively highly complex and extensive matrix damage states here required the human labor time for segmentation to be greater than ~20 h (up to ~70 h) for a given load step, compared to the requirement of ~10–15 h for a given load step in [11], thus limiting which load steps were analyzed here. Future work will focus on analyzing additional load steps. Note that fiber break segmentation was not done given the associated increase in labor requirements versus those of matrix damage. More details are provided in [17].

3 RESULTS AND DISCUSSSION

In this section, the DENT *ex situ* UTS values for the Thin and Thick baseline and nanostitched laminate configurations and 4D progressive damage characterizations associated with *in situ* DENT loading at selected load steps are presented. Note that similar Intmed results are provided in [15].

3.1 Experimental Measurements for *Ex Situ* DENT UTS Calibration

Presented in Table 2 are the *ex situ* DENT testing specimen geometry properties and UTS outcomes for Thin and Thick cross-ply CFRP laminates. A digital caliper was employed to measure specimen geometry properties, and UTS is defined in Equation (1). Summarizing the mean *ex situ* DENT UTS trends, the following nanostitched vs. baseline changes are observed: a +15% for Thick, and -6% for Thin. In Figures 3 and 4, the *ex situ* UTS loading response curves for all Thin and Thick baseline and nanostitched cross-ply specimens are shown. DENT specimens generally failed catastrophically with most of the notched section fragmented during ultimate failure. For Thick baseline, the load-displacement curve features a subcritical failure typically around 80%–90% UTS, followed by as light softening before failure, whereas Thick nanostitched exhibits delayed or suppressed subcritical failure. The subcritical load drops observed in Thick specimens are hypothesized to be caused by significant interlaminar and intralaminar matrix damage progression and significant local load redistribution to the center 0° plies. In contrast, Thin load-displacement curves feature brittle (highly linear) failure for both baseline and nanostitched configurations. Note that the cause of the relatively large stiffness increase in the `NANO-L1' specimen is unclear, but it is hypothesized that possibly slightly misaligned grips could induce slight bending in the specimen gage section and altered friction in the loading system. Though, this behavior was relatively uncommon. The non-linearity at relatively low loads (~200–500 N), which occurs similarly in all configurations, is hypothesized to be caused by grip settling, early matrix damage initiation (likely in the 90° plies), or early progression of manufacturing damage.

Table 2: *Ex situ* testing geometric properties measured for Thin and Thick cross-ply CFRP laminates: thickness t_{DENT} (mean and standard error), ligament width w_{DENT} (mean and standard error), and number of specimens tested *ex situ*. UTS (σ_{UTS}) values (mean and standard error) are also presented.

Ply thickness configuration	**Laminate configuration**	**DENT specimen thickness [mm]**	**DENT specimen ligament width [mm]**	**Number of *ex situ* specimens tested**	**DENT UTS [MPa]**
Thin	Baseline	0.88 ± 0.00	2.31 ± 0.01	5	867.8 ± 14.2
Thin	Nanostitched	0.91 ± 0.00	2.31 ± 0.00	4	815.6 ± 8.7
Thick	Baseline	0.88 ± 0.00	2.31 ± 0.01	5	939.6 ± 9.2
Thick	Nanostitched	0.88 ± 0.00	2.33 ± 0.03	4	1076.3 ± 15.0

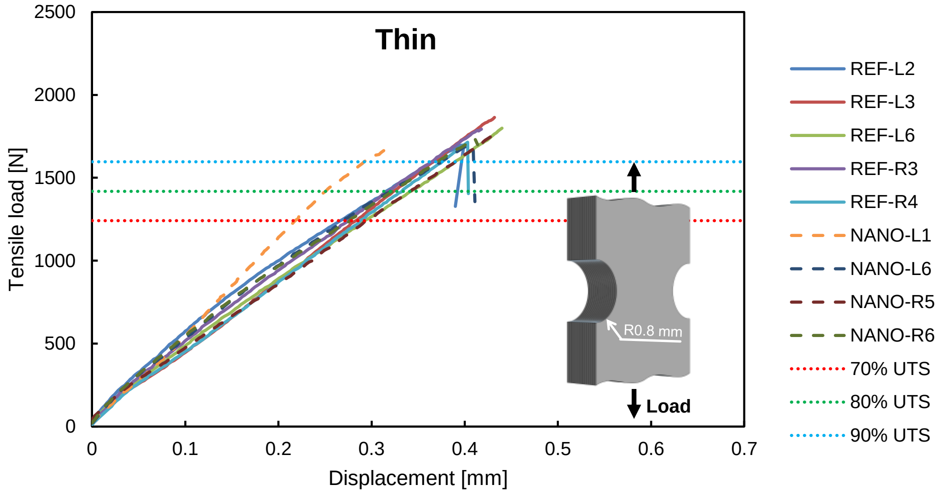

Figure 3: *Ex situ* DENT tensile load-displacement curves for the Thin laminates comprising baseline vs. nanostitched (solid vs. dashed lines, respectively), where different combinations of solid/dashed and line color represent different specimens. Additionally, the 70%, 80%, and 90% UTS load steps (calibrated via mean Thin be-UTS) are shown as dotted lines for reference.

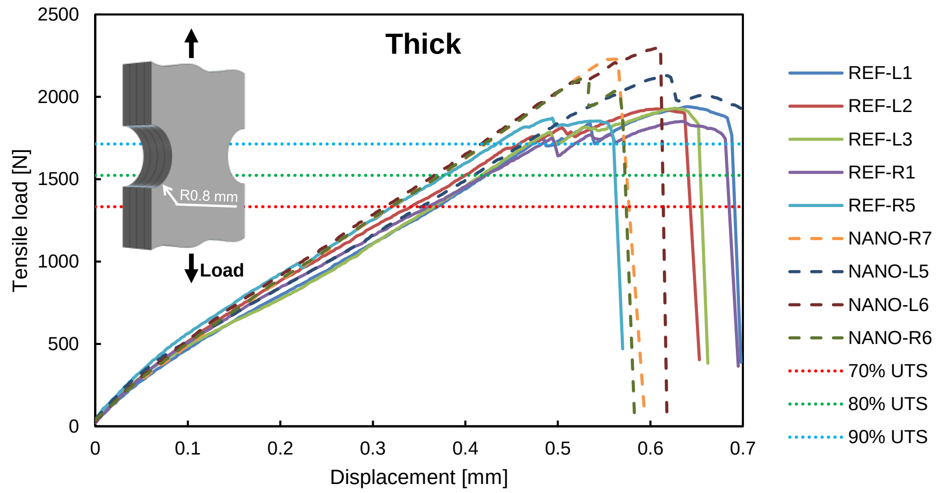

Figure 4: *Ex situ* DENT tensile load-displacement curves for the Thick laminates comprising baseline vs. nanostitched (solid vs. dashed lines, respectively), where different combinations of solid/dashed and line color represent different specimens. Additionally, the 70%, 80%, and 90% UTS load steps (calibrated via mean Thick be-UTS) are shown as dotted lines for reference.

3.2 Experimental Characterization of *In Situ* SRCT/DENT 4D Progressive Damage

Due to time and testing constraints at BL47XU, i*n situ* DENT mechanical testing and SRCT scanning were performed for one specimen of each type (4 types total). The *in situ* DENT load-elapsed time displacement-elapsed time curves, illustrating slight stress-relaxation at each load step, are provided elsewhere [17]. The specimens were taken to failure following the final load step, exhibiting the following *in situ* UTS values: 859.3 MPa for Thin baseline, 811.2 MPa for Thin nanostitched, 896.1 MPa for Thick baseline, and 1184.1 MPa for Thick nanostitched. Shown in Figures 5 and 6 are raw SRCT tomograms from the middle scan region of typical matrix- and fiber-related damage mechanisms in all specimen types at both (approximately the same tomogram location) ~0% UTS (*i.e.*, manufacturing damage) and 90% UTS. The machined notch edge is to the left in these tomograms, and the textured top and bottom exterior surfaces are the result of polymer conforming to the rough peel ply surface during curing. For Thin, observed generally in both specimens are highly diffuse damage mechanisms characterized by intralaminar matrix cracking (small in size, high density), fiber/matrix interfacial debonding, subcritical interlaminar matrix damage (albeit relatively decreased), and fiber breakage. For Thick, observed generally in both specimens are concentrated damage mechanisms characterized by intralaminar matrix cracking (large in size, low density) and fiber/matrix interfacial debonding. For selected load steps of Thin and Thick configurations, *in situ* SRCT visualization of 4D matrix progressive damage is shown next in Figures 7 and 8. Here, matrix damage includes two basic classes: (i) delaminations (interlaminar), and (ii) intralaminar matrix cracks and matrix/fiber interfacial debonds in 0° and 90° plies. Further visualization and geometric quantification of isolated 3D damage modes are shown elsewhere [17], showing, for example, clear delamination suppression by Thick nanostitched.

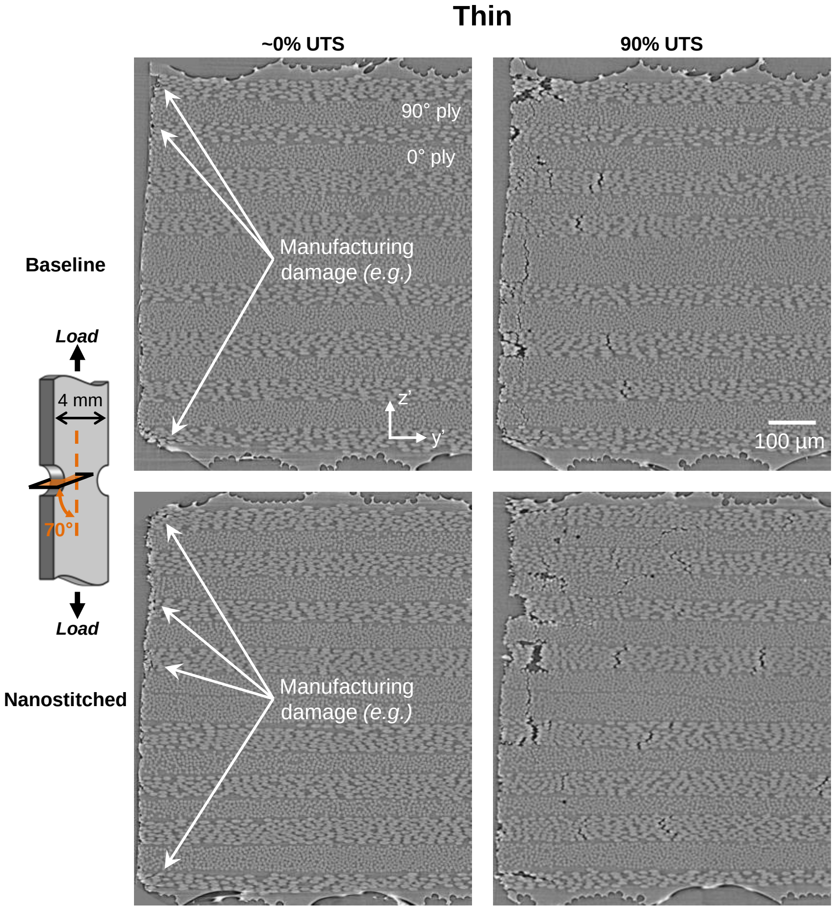

Figure 5: SRCT visualization via raw (unsegmented) tomograms from the middle scan region of typical matrix- and fiber (relatively sparse in Thick)-related damage mechanisms (dark gray to black grayscale intensity) in Thin (top) baseline and (bottom) nanostitched laminates at both (left) ~0% UTS (*i.e.*, manufacturing damage) and (right) 90% UTS (calibrated using mean Thin be-UTS).

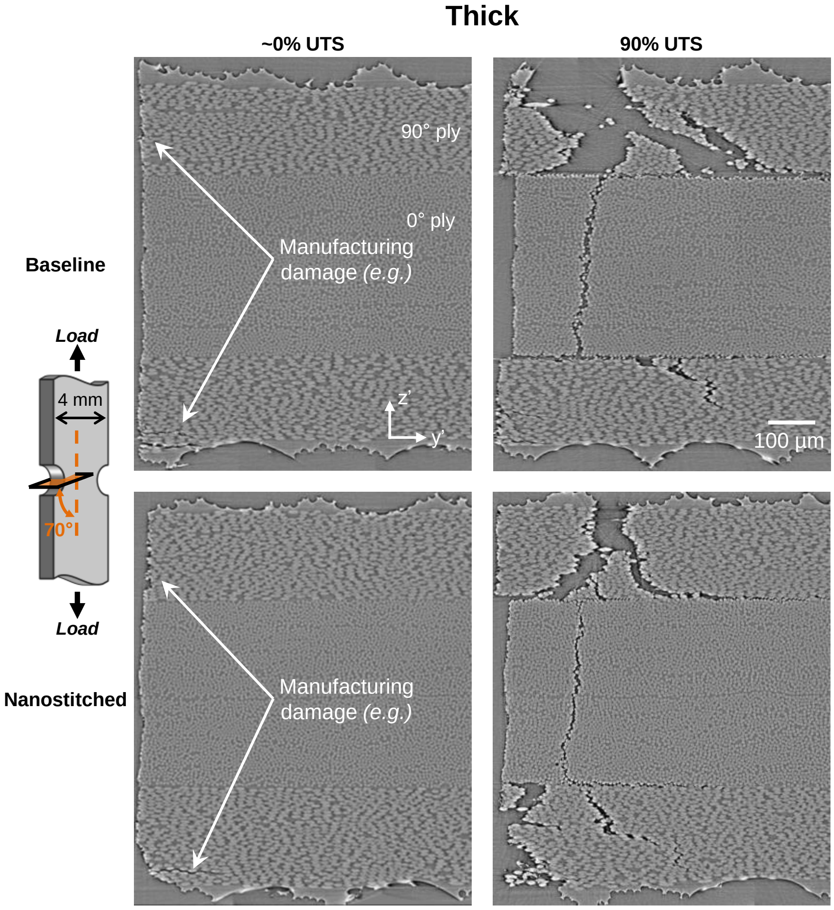

Figure 6: SRCT visualization via raw tomograms from the middle scan region of typical matrix- and fiber-related damage mechanisms (dark gray to black grayscale intensity) in Thick (top) baseline and (bottom) nanostitched laminates at (left) ~0% UTS (manufacturing damage) and (right) 90% UTS.

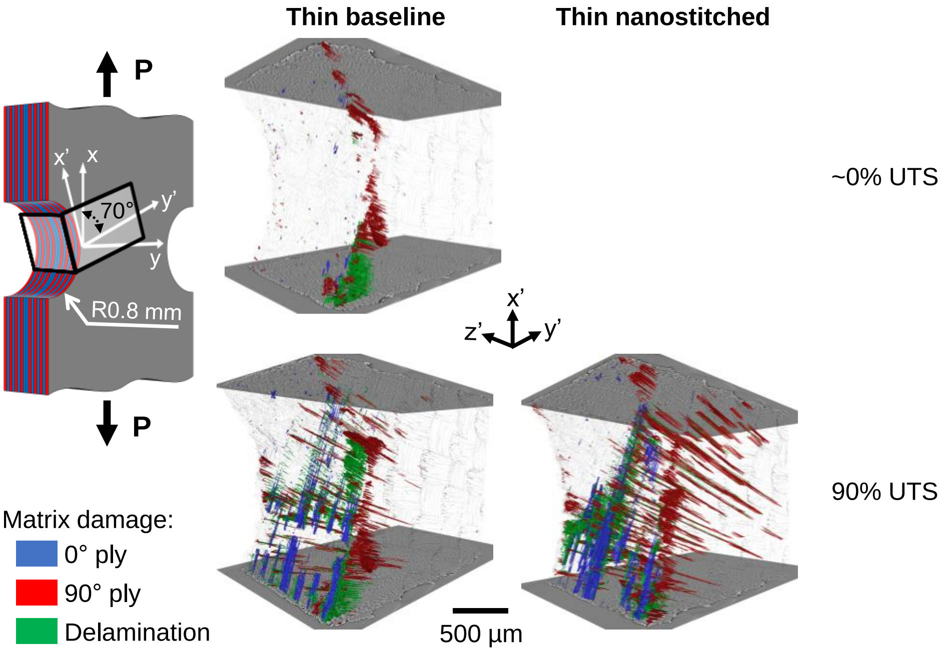

Figure 7: *In situ* SRCT visualization of 3D matrix damage progression in Thin (left) baseline and (right) nanostitched laminates as a function of increasing load. Note that Thin nanostitched at ~0% UTS was not segmented here, but was found to be qualitatively similar to Thin baseline at ~0% UTS.

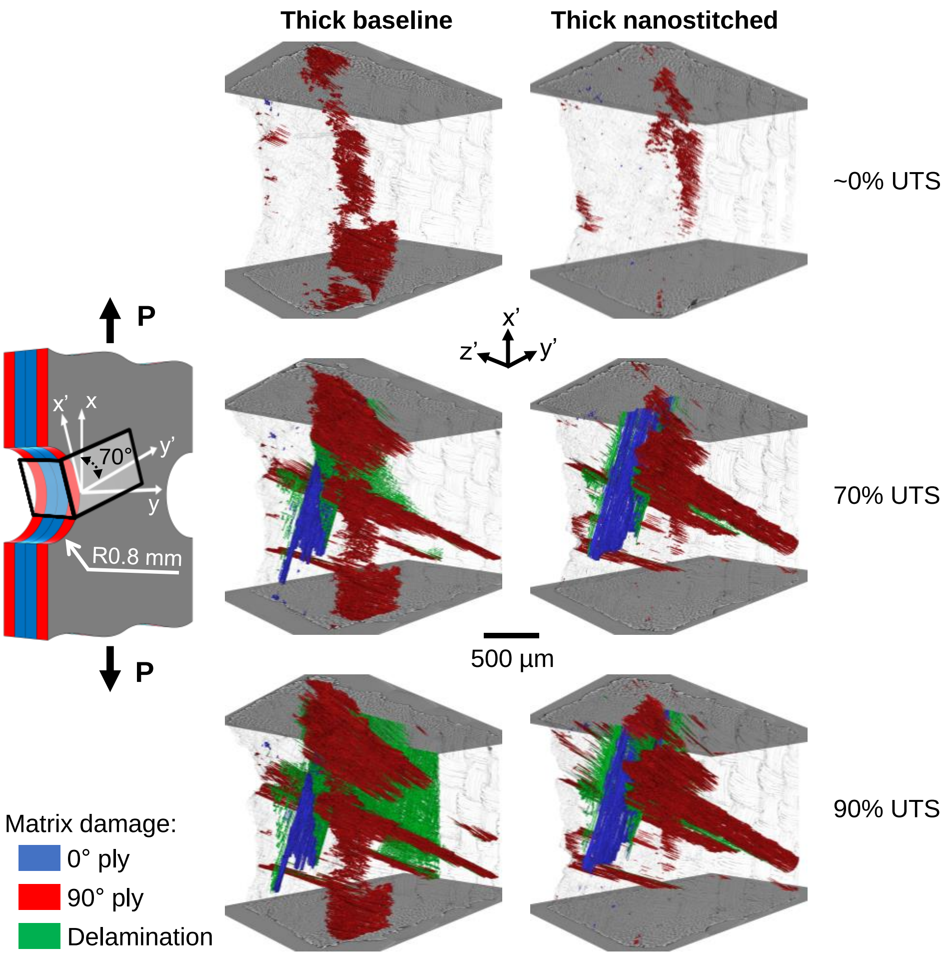

Figure 8: *In situ* SRCT visualization of 3D matrix damage progression in Thin (left) baseline and (right) nanostitched laminates as a function of increasing load.

Consistent with the *'in situ'* size effect [8–10], Thick laminates exhibit large-scale full-ply intralaminar matrix cracking, as well as large delaminations in the baseline that are largely suppressed in nanostitched, which can explain the UTS increase. Specifically, a 4.3× reduction (see for [17] quantitative values) in delamination/interlaminar matrix damage surface area is measured at 90% UTS (interestingly, following a much smaller relative decrease in nanostitched vs. baseline delamination/interlaminar matrix damage surface area measured at 70% UTS), which has not been experimentally possible to date, in the Thick nanostitched specimen relative to the baseline, which strongly underpins and explains its observed highest overall UTS, due to the demonstrated coupling in Thick nanostitched of delamination suppression and a strong notch blunting effect. In contrast, Thin laminates exhibit a minor extent of diffuse damage, which may be beneficial in fatigue loading, consisting of a blend of fiber breaks, fiber/matrix interfacial debonding, and sub-ply and full-ply intralaminar matrix cracking, and small subcritical delaminations, corroborating the absent nanostitch effect on UTS and the lowest UTSs (due to the lack of stress redistribution around the notch edge stress concentration, as in found in [11]). Interestingly, the Thin nanostitched specimen appears to show considerably more overall matrix damage than the baseline in this cross-ply notched tension configuration, consistent with the observed 6% *ex situ* UTS decrease, which may potentially be attributed to differences in behavior during manufacturing (*e.g.*, potential elevated brittleness) of these Thin nanostitched laminates or local complex alterations of the stress state relative to the that of the baseline. By comparison, as reported in [15], Intmed laminates display a mix of full-ply intralaminar matrix cracking, subcritical delaminations, and relatively sparse fiber breakage, signifying a transition between matrix (Thick)- and fiber (Thin)-dominated failure modes and resulting interestingly in Intmed having a higher baseline DENT UTS than that of the Thin or Thick baseline specimen.

4 CONCLUSIONS

A-CNTs were embedded in the ply/ply interfaces of DENT specimens comprised of cross-ply aerospace-grade carbon fiber reinforced epoxy laminates consisting of two different ply thickness (achieved via ply blocking of thin-ply laminae), followed by uniaxial tensile loading in a canted rig and *in situ* SRCT scanning at various load steps to non-destructively image 3D damage state evolution. The highest ultimate tensile strength (UTS) among all specimen types was achieved by the Thick nanostitched specimens (15% increase over Thick baseline, >20% increase over Thin specimens), which demonstrated an effective combination of notch-blunting intralaminar matrix damage and suppressed interlaminar matrix damage (4.3× less surface area at 90% UTS). Regarding ply thickness effects (baseline specimens), an 8% UTS increase was exhibited in Thick specimens over the Thin specimens, which is substantiated mechanistically by the observed characteristic progressive damage states being dominated in thick-ply laminates by notch-blunting inter- and intra-laminar matrix damage and in thin-ply laminates by brittle fiber breakage- and diffuse matrix damage. Altogether, these novel experiments contribute to new fundamental understanding of complex 4D failure mechanisms of the two emerging mechanical enhancement technologies studied here, which is valuable for achieving potential synergistic property improvements in hybrid laminates and informing present modeling limitations. Future work will include segmentation of additional load steps and *in situ* SRCT scanning closer to ultimate failure.

ACKNOWLEDGEMENTS

This work was supported by Airbus, ANSYS, Boeing, Embraer, Lockheed Martin, Saab AB, and Teijin Carbon America through MIT's Nano-Engineered Composite aerospace STructures (NECST) Consortium, and by National Funds through FCT – Fundação para Ciência e a Tecnologia in the scope of project MITP-TB/PFM/0005/2013. This work made use of facilities supported in part by the U.S. Army Research Laboratory and the U.S. Army Research Office through the Institute for Soldier Nanotechnologies, under contract number W911NF-13-D-0001, the facilities at the U.S. Army Natick Solider R, D & E Center (NSRDEC), and was carried out in part through the use of MIT's Microsystems Technology Laboratories (MTL). Micro-computed tomography instrumentation support by the Office of Naval Research (ONR) under grant number ONR.N000141712068 through the Defense University Research Instrumentation Program (DURIP) is gratefully acknowledged. For the first author, this material is based upon work supported by the National Science Foundation Graduate Research Fellowship Program under Grant No. 1122374. Any opinions, findings, and conclusions or recommendations expressed in this material are those of the author(s) and do not necessarily reflect the views of the National Science Foundation. The third author would like to thank Fundação para a Ciência e a Tecnologia (FCT), grant SFRH/BD/115859/2016. We thank Sebastian Rosini and Ronan Smith of the University of Southampton, UK for providing support at beamline 47XU. All authors thank the necstlab at MIT and lab members at μ-VIS X-Ray Imaging Center at University of Southampton for discussion and input. The authors thank Teijin Carbon America for the donation of thin-ply prepreg materials.

REFERENCES

[1] I.K. Partridge, D.D.R. Cartié, Delamination resistant laminates by Z-Fiber® pinning: Part I manufacture and fracture performance, Composites Part A: Applied Science and Manufacturing. 36 (2005) 55–64. doi:10.1016/j.compositesa.2004.06.029.

[2] I.K. Partridge, S.R. Hallett, Use of microfasteners to produce damage tolerant composite structures, Philosophical Transactions of the Royal Society A: Mathematical, Physical and Engineering Sciences. 374 (2016) 20150277. doi:10.1098/rsta.2015.0277.

[3] L. Tong, A. Mouritz, M. Bannister, 3D Fibre Reinforced Polymer Composites, Elsevier, 2002. doi:10.1016/B978-0-08-043938-9.X5012-1.

[4] R. Guzman de Villoria, P. Hallander, L. Ydrefors, P. Nordin, B.L. Wardle, In-plane strength enhancement of laminated composites via aligned carbon nanotube interlaminar reinforcement, Composites Science and Technology. 133 (2016) 33–39. doi:10.1016/j.compscitech.2016.07.006.

[5] B.G. Falzon, S.C. Hawkins, C.P. Huynh, R. Radjef, C. Brown, An investigation of Mode I and

Mode II fracture toughness enhancement using aligned carbon nanotubes forests at the crack interface, Composite Structures. 106 (2013) 65–73. doi:10.1016/J.COMPSTRUCT.2013.05.051.

[6] X. Ni, C. Furtado, N.K. Fritz, R. Kopp, P.P. Camanho, B.L. Wardle, Interlaminar to intralaminar mode I and II crack bifurcation due to aligned carbon nanotube reinforcement of aerospace-grade advanced composites, Composites Science and Technology. 190 (2020) 108014. doi:10.1016/j.compscitech.2020.108014.

[7] K. Kawabe, S. Tomoda, T. Matsuo, Pneumatic process for spreading reinforcing fiber tow, in: International SAMPE Symposium and Exhibition (Proceedings), 1997: pp. 65–76. https://www.scopus.com/inward/record.uri?eid=2-s2.0-0030719589&partnerID=40&md5=1a2998a96b72aae5587902e3b1b66023.

[8] C.C. Chamis, T.L. Sullivan, In situ ply strength: An initial assessment, NASA TM-73771. (1978).

[9] P.P. Camanho, C.G. Dávila, S.T. Pinho, L. Iannucci, P. Robinson, Prediction of in situ strengths and matrix cracking in composites under transverse tension and in-plane shear, Composites Part A: Applied Science and Manufacturing. 37 (2006) 165–176. doi:10.1016/j.compositesa.2005.04.023.

[10] A. Arteiro, C. Furtado, G. Catalanotti, P. Linde, P.P. Camanho, Thin-ply polymer composite materials: A review, Composites Part A: Applied Science and Manufacturing. 132 (2020) 105777. doi:10.1016/j.compositesa.2020.105777.

[11] X. Ni, R. Kopp, E. Kalfon-Cohen, C. Furtado, J. Lee, A. Arteiro, G. Borstnar, M.N. Mavrogordato, L. Helfen, I. Sinclair, S.M. Spearing, P.P. Camanho, B.L. Wardle, In situ synchrotron computed tomography study of nanoscale interlaminar reinforcement and thin-ply effects on damage progression in composite laminates, Composites Part B: Engineering. (2021) 108623. doi:10.1016/j.compositesb.2021.108623.

[12] E. Kalfon-Cohen, R. Kopp, C. Furtado, X. Ni, A. Arteiro, G. Borstnar, M.N. Mavrogordato, I. Sinclair, S.M. Spearing, P.P. Camanho, B.L. Wardle, Synergetic effects of thin plies and aligned carbon nanotube interlaminar reinforcement in composite laminates, Composites Science and Technology. 166 (2018) 160–168. doi:10.1016/j.compscitech.2018.01.007.

[13] P. Wright, A. Moffat, I. Sinclair, S.M. Spearing, High resolution tomographic imaging and modelling of notch tip damage in a laminated composite, Composites Science and Technology. 70 (2010) 1444–1452. doi:10.1016/j.compscitech.2010.04.012.

[14] A.J. Moffat, P. Wright, J.Y. Buffière, I. Sinclair, S.M. Spearing, Micromechanisms of damage in 0° splits in a [90/0]scomposite material using synchrotron radiation computed tomography, Scripta Materialia. 59 (2008) 1043–1046. doi:10.1016/j.scriptamat.2008.07.034.

[15] R. Kopp, X. Ni, C. Furtado, J. Lee, E. Kalfon-Cohen, K. Uesugi, M. Kinsella, M.N. Mavrogordato, I. Sinclair, S.M. Spearing, P.P. Camanho, B.L. Wardle, In Situ Synchrotron X-ray Microtomography of Progressive Damage in Canted Notched Cross-Ply Composites with Interlaminar Nanoreinforcement, in: AIAA SCITECH 2022 Forum, American Institute of Aeronautics and Astronautics, Reston, Virginia, 2022: pp. 1–19. doi:10.2514/6.2022-0375.

[16] S. Wilby, M.N. Mavrogordato, I. Sinclair, S.M. Spearing, Identifying Strains Associated With Crack Initiation in Carbon Fibre, in: 3rd International Conference on Tomography of Materials and Structures, Lund, Sweden, 2017: pp. 8–10. https://meetingorganizer.copernicus.org/ICTMS2017/ICTMS2017-46.pdf.

[17] R. Kopp, X-ray Micro-Computed Tomography and Deep Learning Segmentation of Progressive Damage in Hierarchical Nanoengineered Carbon Fiber Composites, Massachusetts Institute of Technology, 2021. https://dspace.mit.edu/handle/1721.1/138357.

[18] E.J. Garcia, B.L. Wardle, A. John Hart, Joining prepreg composite interfaces with aligned carbon nanotubes, Composites Part A: Applied Science and Manufacturing. 39 (2008) 1065–1070. doi:10.1016/j.compositesa.2008.03.011.

[19] S. Sihn, R.Y. Kim, K. Kawabe, S.W. Tsai, Experimental studies of thin-ply laminated composites, Composites Science and Technology. 67 (2007) 996–1008. doi:10.1016/j.compscitech.2006.06.008.

[20] K. Uesugi, M. Hoshino, A. Takeuchi, Y. Suzuki, N. Yagi, T. Nakano, Development of fast (sub-minute) micro-tomography, AIP Conference Proceedings. 1266 (2010) 47–50. doi:10.1063/1.3478197.